RSC Advances

ROYAL SOCIETY OF CHEMISTRY

www.rsc.org/advances

A Pair of Bubbles Rising Dynamics in Xanthan Gum Solution: A CFD Study

Md. Tariqul Islam, P. Ganesan*, Ji Cheng

Department of Mechanical Engineering, University of Malaya, 50603 Kuala Lumpur, Malaysia

Abstract

The motion and interaction of a bubble pair in a non-Newtonian fluid (xanthan gum solution) were numerically simulated using volume of fluid (VOF) method, in which the continuous surface tension model and the power-law model were adopted to represent surface tension and rheological properties of non-Newtonian fluids, respectively. The effects of initial horizontal bubble interval, oblique alignment and rheological properties of non-Newtonian fluids on a pair of bubbles rising side-by-side were evaluated in this study. The results indicated that for the case with non-dimensional initial horizontal interval of bubble h* = 4.0, the interaction between the bubbles shows a minimum repulsive effect. Moreover, for the oblique angle alignment a greater repulsive force between the bubbles was seen when the angle was reduced. However, oblique coalescence occurred due to the higher attraction between the bubbles at higher angle, which is independent of flow index It is also found that the repulsion effect as well as the variation of the bubble shape from spherical to wobbling are more significant at a lower flow index ($n < 0.5$) due to the shear-thinning effect as well as the differences of their flow field structures.

Keywords: VOF; xanthan gum; bubble rise trajectory.

* Corresponding author

E-mail address: poo_ganesan@um.edu.my

Nomenclature

$\vec{D}$	strain rate tensor, N/m
Fs	body force, N/m^3
F	volume fraction function
g	gravitational acceleration, m/s^2
K	consistency coefficient, $Pa \cdot s^n$
n	flow index
$\hat{n}$	normal vector
$\vec{n}$	unit normal vector
P	pressure, Pa
d_o	initial bubble diameter, mm
d_e	equivalent bubble diameter, mm
d_h	bubble height as considered shorter bubble diameter, mm
d_w	bubble width as considered larger bubble diameter, mm
H	column height, mm
h	bubble position in the column, mm
Re	Reynolds number
ΔX	actual distance between bubbles, mm
Xi	initial distance between bubbles, mm
h*	non-dimensional horizontal interval, [-]
t	time, s
$\vec{V}$	velocity vector, m/s

U_T terminal velocity, m/s

Greek symbols

θ angle between the centreline of bubbles and the horizontal direction, (^{o})

$\dot{\gamma}$ shear rate, 1/s

τ shear stress, Pa

μ viscosity, Pa·s

μ (F) kinematic viscosity coefficient, m^2/s

ρ density, kg/m^3

σ surface tension, N/m

k interfacial curvature between gas and liquid

Subscript

g gas phase

l liquid phase

1. Introduction

The bubble column reactor is a device in which gas is usually dispersed as bubbles which rise through the liquid. The overall performance of a bubble column mainly depends on the bubble flow characteristics, bubbles coalescence and bubble break up phenomenon which alters the bubble size distribution and enhances the gas−liquid contact area by the action of vortices via stretching, tearing etc., resulting a significant increase in heat and mass transfer and chemical reaction rate. [1-3] Nowadays, the bubble column reactors are widely used as gas-liquid interface equipments in various industrial sectors such as chemical, petrochemical, pharmaceutical, etc.,

involving reactions such as oxidation, chlorination, alkylation, polymerization and hydrogenation, and eventually they are employed as bioreactors to produce valuable products like enzymes, proteins, antibiotics, etc. [1, 2] Recently, a number of experimental and theoretical studies [4-10] have been done on formation and rise characteristics of single bubble in stagnant fluids under the buoyancy force in Newtonian fluids. The literature has provided almost entire information regarding a single bubble formation and rise characteristics. However, in industrial environments, the swarm bubbles or multiple bubbles are commonly encountered than the single bubble. Thus, the obtained information on the single bubble might not be broadened to the multiple bubble systems. On the other hand, most of materials encountered in both nature and industry are non-Newtonian fluids. Compared to Newtonian fluids, the non-Newtonian fluids usually show many peculiar properties, for instance, shear-thinning, viscoelasticity, rod-climbing and tubeless siphon. [11-13] Hence, the bubble rising behavior and interaction in non-Newtonian fluids are more complex and also the relevant researches are quite rare. Therefore, the fundamental knowledge of bubble rising behavior and interactions in non- Newtonian fluids could be more scientific to make sure the modeling of gas–liquid flow in bubble column. [14, 15]

Most of the experimental studies have focused on single or in-line bubble rise dynamics in non-Newtonian fluids. [16-19] For example, Hassagar [16] investigated the two in-line bubble rise dynamics in non-Newtonian fluids. It was found that a negative wake encouraged by elasticity pushes the liquid away from the bubble. Lin et al. [17] also found that for two in-line bubbles, the acceleration of the trailing bubble to the leading bubble is caused by negative pressure; and the shear-thinning effect in addition to the pushing force is caused by viscoelastic effect. Hassan et al.

[20] investigated the bubble zigzag trajectory with maximum amplitude for lower size of bubble in low xanthan gum concentration solution.

Few attempts have been made to investigate experimentally the interaction between bubble pairs rising side-by-side in non-Newtonian fluids. [21-24] Sanada et al. [21] experimentally investigated the motion of a horizontally aligned pair of rising bubbles in silicone oil. They found that the velocities of the bubbles decrease after coalescence by as much as 50% when the bubbles rising side-by-side bounce off each other. The bubble repulsion effect was observed due to a large amount of fluid in the space between bubbles, which resulted in the bubbles movement in a direction away from each other. Vélez-Cordero et al. [23] experimentally investigated the interaction of two bubbles rising in shear-thinning fluids of xanthan gum solution ($0.55 < n < 1.0$). They observed that the attractive motion between the bubbles was increased with the amount of shear-thinning (decreasing the flow index). The bubble pairs showed an oscillatory motion due to the reduced viscosity behind the leading bubble. Fan et al. [24] focused on the rise and interaction between two parallel rising bubbles by analyzing the velocity field around bubbles using particle image velocimetry (PIV), and found that within certain distance between two bubbles, the interaction between two neighboring bubbles change from mutual repellence to attraction with decreasing the angle of line which links the two bubbles' centers to the vertical direction. Legendre et al. [22] investigated the two parallel spherical bubbles rising behavior in a viscous fluid. They reported that the hydrodynamic interactions between the bubbles would be cohesive or repulsive that primarily depends on Reynolds number.

Recently, more and more researchers [25-35] make use of various numerical methods such as Volume of Fluid method (VOF), Level Set method (LS), Lattice Boltzmann method (LB), and

Front Tracking method (FT) to investigate bubble dynamics or interactions. In general, their results were in a reasonable agreement with the existing experimental data. Fan et al. [25] successfully analyzed two bubbles rising dynamics side-by-side in concentrated carboxymethyl cellulose (CMC) solution by using VOF method. The results showed a good agreement with the experimental measurements. They found that the repulsive effect between two bubbles decreases with increasing the initial center-to-center distance of bubbles and increase of the oblique angle between them. Similarly, Yu et al. [26] investigated two parallel bubbles rising behavior in viscous fluid using adaptive LB method. The authors found that the repulsive behavior of two spherical bubbles occurs at lower Reynolds number, but cohesive behavior and finally coalescence of the bubbles at higher Reynolds numbers. Li Zhang et al [28] studied the motion of a single bubble rising freely through CMC sodium salt, sodium hydroxyl-ethyl cellulose (HEC) and xanthan gum (XG) solution using a level set method for tracking the bubble interface. They investigated the shear rate and viscosity distribution and shape of a bubble rising in CMC, HEC, XG solution and compare to sodium acrylate polymer (SAP) shear-thinning solution. Liu et al. [32] performed a numerical investigation on three equal intervals parallel bubbles rising in CMC non-Newtonian fluids. The governing equations were solved using VOF method. It was seen that the three parallel bubbles would be coalesced when the horizontal interval between the bubbles was less than 1 mm, otherwise the bubbles would experience a repulsive effect.

In summary, a detailed study of a bubble pair rise dynamics in a pure concentrate of xanthan gum solution (i.e., non-Newtonian) with shape changes is not available to the best the authors' knowledge. There are few works in which xanthan gum mixture solutions (xanthan-glycerin/water) are tested, which has a different physical property from the pure concentrate of xanthan gum

solution, e.g., see Refs. [20, 23] The present study provides detailed information on a pair bubble rising dynamics and shows how the shape of the bubbles evolves with time in a pure concentrate of xanthan gum solution. Specifically, a pair of 6 mm bubble rise dynamics with different initial configurations in such concentrate of non-Newtonian fluid is studied. The effects of initial horizontal bubble interval distance, non-horizontal configurations, rheological properties of shear thinning fluids is simulated in detail using the VOF method to study the interactions between bubble pairs and the flow field structures and pressure distribution around the bubbles. The knowledge from the present study could be useful for multi-scale approach to predict bubble swarm behavior as well as to improve the understanding of the mechanisms of multiple bubble rise dynamics. [31]

2. Numerical methods

In this work, the continuous surface tension model and the rheological properties of non-Newtonian fluids are incorporated into the VOF method to a pair of bubbles rising in shear-shinning fluids.

2.1 Physical Model

The physical model of the simulation was simplified to a 2D computational domain with the dimension of 120 mm height and 90 mm width, as shown in Fig. 1a. The bottom and two side of the domain are assigned as no slip wall boundary conditions. The top of the domain is assigned as pressure outlet boundary condition. The operating pressure is set to be equal to the ambient pressure, i.e., 101325 Pa and the gravitational force (g) of -9.81 m/s^2 is assigned along y-axis. At

the initial stage of simulation, a pair of bubbles with a diameter of 6 mm is imposed at the centre and 12 mm height from the bottom of the domain. The bubbles in quiescent non-Newtonian fluids rise under the action of buoyancy and the bubbles rising dynamics are numerically investigated. The effect of the column wall to the bubble is negligible since the bubble size is small in comparison to the column width. In the present study, xanthan gum solution is used as the non-Newtonian fluid. The non-Newtonian fluid data are taken from Hassan et al. [20] The non-Newtonian fluid has the following properties: density, ρ_l = 997.0 kg/m^3 and surface tension, σ = 0.063 N/m. Rheological data of consistency coefficient K = 0.095 Pa.s^n and flow index n = 0.548 were used to fit the power-law model.

2.2 Governing equations

2.2.1 Equations of continuity and momentum

The continuity and momentum equations for an incompressible fluid can be written as [36]:

$$\nabla.\vec{\mathrm{V}} = 0 \tag{1}$$

$$\rho(F)\left(\frac{\partial\vec{\mathrm{V}}}{\partial t} + \nabla\vec{\mathrm{V}}.\vec{\mathrm{V}}\right) = -\nabla P + \rho(F)\vec{\mathrm{g}} + \nabla.\left[\,2\mu(F)\vec{\mathrm{D}}\,\right] + \vec{\mathrm{F}}\mathrm{s} \tag{2}$$

where ρ is fluid density; $\vec{\mathrm{V}}$ is the velocity vector of fluid; P is pressure; $\vec{\mathrm{F}}$s is body force; μ is dynamic viscosity coefficient. Strain rate tensor, $\vec{\mathrm{D}}$ is written as below:

$$\vec{\mathrm{D}} = \frac{1}{2}\left(\nabla\vec{\mathrm{V}} + \nabla\vec{\mathrm{V}}^T\right) \tag{3}$$

The local averaged density ρ (F) and kinematic viscosity coefficient μ (F) are evaluated from the local distribution of the phase volume function F:

$$\rho(F) = \rho_l(F) + \rho_g[1 - F] \quad (4)$$

$$\mu(F) = \mu_l(F) + \mu_g[1 - F] \quad (5)$$

where ρ_l and ρ_g, are the density of liquid and gas, and μ_l and μ_g are the viscosity of liquid and gas respectively. The volume fraction (F) is defined as the fraction of the liquid inside a control volume or cell, in which F taking the value of 0 for pure gas cell; 1 for pure liquid cell and between 0 and 1 for interface of gas and liquid in the cell. The volume fraction equation is defined as follows [37]:

$$\frac{\partial F}{\partial t} + \nabla.\left(\vec{\mathrm{V}}\, F\right) = 0 \quad (6)$$

2.2.2 Source term of momentum equation induced by surface tension

Surface tension has important impact on the interface because the minor curvature of a bubble could generate major additional pressure. The continuum surface force (CSF) is used to calculate the gas-liquid interface motion, which is incorporated as a source term in the momentum equation (Eq. 2) by introducing a body force $\vec{\mathrm{F}}\mathrm{s}$ as described by Brackbill et al. [38] This body force is calculated by the following equation:

$$\vec{\mathrm{F}}\mathrm{s} = \sigma\, \frac{\rho\, k\, \nabla F_l}{0.5\,(\rho_l + \rho_g)} \quad (7)$$

where, F_l is liquid phase fraction; k is liquid phase fraction and the surface curvature of the interface, which is defined in term of divergence of the normal vector, $\hat{n}$ and it is calculated by using the following equation:

$$k = -(\nabla.\hat{n}) = \frac{1}{|\vec{n}|}\left[\left(\frac{\vec{n}}{|\vec{n}|}\cdot\nabla\right)|\vec{n}| - (\nabla\cdot\vec{n})\right] \text{ ; Where } \hat{n} = \frac{\vec{n}}{|\vec{n}|} \quad (8)$$

2.2.3 Constitutive equation of continuous phase

In non-Newtonian fluid, the shear-thinning effect is presented by power-law model [39]:

$$\mu(F) = K\dot{\gamma}^{n-1} \tag{9}$$

where K and n are the consistency coefficient and flow index of shear-thinning fluids, respectively. The viscosity μ could be obtained from the local shear rate $\dot{\gamma}$ which could be written as below:

$$\dot{\gamma} = \sqrt{2(\vec{\mathrm{D}}:\vec{\mathrm{D}})} \tag{10}$$

Therefore, the viscosities of non-Newtonian fluids could be obtained by combination of equation (3), (9) and (10).

2.3 Model validation

2.3.1 Grid analysis

A uniform structured mesh is used for the present study, as shown in Fig. 1b. Fig. 2 shows the effect of mesh interval sizes (0.15, 0.25, 0.35 and 0.45 mm) on the simulation results of single bubble rising velocities with initial diameter of 6 mm in the xanthan gum solution. The density, surface tension, consistency coefficient and flow index of power-law fluid were 997.0 kg/m^3, 0.064 N/m, 0.095 Pa.s^n and 0.548, respectively. [20]. It could be found that the single bubble rising velocities at mesh interval size 0.25 mm are almost the same as that of 0.15 mm. Therefore, the mesh interval size 0.25 mm was adopted throughout this study to take into accounts both the computational accuracy and the time consumption. Similarly, satisfactory simulation results were

obtained between the current study and the one done by Ma et al. [40] for the influence of different factors on the single bubble formation and bubble dynamics with mesh interval size 0.25 mm.

2.3.2 Code validation

In order to validate the reliability of the computational method, two types of study have been considered. First, the processes of two parallel bubbles rising in carboxymethyl cellulose sodium (CMC) solution were simulated and the results agreed well as compared to the experimental results [32], as depicted in Fig. 3a-b. The density, surface tension, rheological parameters of consistency coefficient and flow index of CMC aqueous solution are 1005.6 kg/m^3, 0.06875 N/m, 0.048 Pa.s^n and 0.922 respectively. For the second validation, a single bubble with the initial diameters of 6 mm and 10 mm in the present of non-Newtonian fluids (i.e., xanthan gum solution) were simulated and compared with experimental results reported in [20]. The relative error of Reynolds numbers were about 2.43% and 1.22% for the initial diameters of 6 mm and 10 mm, respectively. The Reynolds number is calculated as [32, 41, 42]:

$$\mathrm{Re} = \frac{\rho_l d_e^n U_T^{2-n}}{K} \tag{11}$$

where $d_e = [(d_h \times d_w^2)^{1/3}]$ [20] and U_T is the equivalent diameter and the bubble terminal velocity, respectively. The equivalent (d_e) was calculated using the short bubble diameter (d_h) and larger bubble diameter (d_w) of the elliptic bubble after reached steady conditions or no more variation of the instantaneous bubble velocity.

The relative errors of Reynolds number was found about 3.76% for the two parallel bubbles. Therefore, the above comparison results indicated that the VOF computational method can be reliable to predict the present investigation.

2.4 Numerical procedures

In this study, the CFD code, FLUENT, was used to solve the governing equations employing pressure based solver. The pressure–velocity coupling equation was solved using the pressure implicit with splitting of operators (PISO) algorithm. The geometric reconstruction approach was adopted to track the interface between two phases using a piecewise linear interface calculation (PLIC) method. [43] Discretization scheme of pressure and momentum were pressure staggering option (PRESTO!) and second order upwind, respectively. The iteration and time steps were 1.0E-6 and 0.0001s, respectively. At the beginning, initial spherical bubbles were patched at the bottom of the computational domain containing only quiescent liquid.

2.5 Simulation cases

A total of 17 simulation cases were carried out. The first two cases were done for the validation purpose, in which the bubbles with diameters of 4 mm (Case 1) and 6 mm (Case 2 were set to rise from a rest condition with the initial position of 12 mm vertical height from the bottom of the computational domain. Three cases (Cases3-5) were used to investigate the effect of non-dimensional horizontal intervals (i.e., h* = 1.5, 2.0 and 4.0) between a pair of bubbles with d_o = 6 mm. The non-dimensional horizontal interval is defined as h* = Xi/d_o, where Xi is the initial distance between the centres of bubbles pair and d_o is the initial bubble diameter. Cases 6-8 were

used to investigate the effect of flow index (n) on non-Newtonion fluid between the bubbles pair rising dynamics. In Cases 9-17, the effect of oblique angle (θ) and flow index (n) on fluid flow were studied. A summary of all the simulation cases is given in Table 2.

3. Result and Discussion

3.1 Effect of different initial horizontal interval between a pair of bubbles

Bubbles pair rising dynamics in horizontal direction are closely related to the initial horizontal bubble interval and the physical properties of non-Newtonian fluids. The interaction of bubbles pair is investigated with three different non-dimensional initial horizontal intervals h* = 1.5, 2.0 and 4.0. Fig. 4 shows the 6 mm bubbles pair rising trajectories with three different initial bubble intervals. The results reveal that the path, shape as well as velocity experience a significant variation with increasing the distance between the centres of the two bubbles. The bubble shape changes from spherical to wobbling shape (or irregular shape) for the three different initial bubble intervals. The bubbles pair rising trajectory is asymmetric along the perpendicular line in the middle of the vertical column, as can be seen from Fig. 4. For h* = 1.5 (see Fig. 4a) and h* = 2.0 (see Fig. 4b), a stronger repulsive interaction between two parallel bubbles is observed rather than the interval of h* = 4.0 (see Fig. 4c). Consequently, the results for bubble horizontal interval ratio, bubble aspect ratio (or the ratio of minimum to maximum deformation of bubble), bubble rising velocity and static pressure on bubble as a function of time at three different initial bubble intervals are shown in Fig. 5a, 5b, 5c and 5d, respectively.

According to Fig. 5a, the highest variation of bubbles rising trajectory, in horizontal direction, occurs for the low initial bubble intervals of h* = 1.5 and 2.0. This is due to the stronger

effect of repulsion as a result of large amount of vortices generated between the bubbles interval. While in the case of h* = 4.0, the bubble rising trajectory in horizontal direction remains less fluctuated, indicating the weak repulsion effect. This results is in agreement with the experimental work of Vélez-Cordero et al. [23] Consequently from Fig. 5b, for h* = 1.5, the curve of bubble aspect ratio was fluctuated intensely, but less fluctuation was observed in h* = 2.0 curve. When the initial interval increased to h* = 4.0, the variation of bubble shape was not varied so significantly compared to the other non-dimensional intervals. The change of bubble aspect ratio occurs due to the stronger vortexes field lying in the gap between bubbles pair that keep interacting with each other and also the interacting force in the horizontal direction which varies with time. Meanwhile, it is also worth noting that the bubbles rising velocity depends on the distance between bubbles, as can be observed in Fig. 6a and 6b. As can be seen in Fig. 5c, the bubbles pair with initial interval h* = 4.0 was observed to reach the terminal velocity 0.16 m/s, which is higher than those with h* = 2.0 and 1.5. It means that the vertical motion of bubbles with small distance is weakened by their repulsive effect in horizontal direction, and the terminal velocity of bubbles pair would increase with the increase of initial bubble interval due to weaker vortex field between the bubbles gap, as can be observed in Fig. 6c. So it is reasonable to conclude that bubble-bubble interaction exhibits a repulsive effect, which decreases with the increase of distance between bubbles and the repulsive effect can be considered negligible at h* $\geq$ 4. On the other hand, the effect of initial bubble intervals on bubble static pressure, which is calculated as, P = (H-h) ρ g, where H is height of the bubble column, h is the height to which the bubble had risen. The results are shown in Fig. 5d. It is found that the static pressure on the

bubble decreases with increase of h* and time. In comparing the value of h* = 1.5 and 4.0, on average, the drop of the static pressure is about 30%.

3.2 Effect of flow index on a pair of bubbles rise dynamics

Flow index n reflects the deviating degree of non-Newtonian fluids from Newtonian fluids (n = 1). Most non-Newtonian fluids are pseudo plastic with $0 < n < 1$. If n is less than one, the power law (Eq. 9) predicts that the effective viscosity would decrease with increasing shear rate. The simulation was done by setting different flow index; however the other properties such as air bubble density and the density of liquid, surface tension, column shape and the consistency of the fluid were kept constant. In this study, the three different flow indexes (n = 0.1, 0.5 and 0.9) were taken into consideration to see the effect of flow index on bubbles rising dynamics in non-Newtonian fluid. Fig. 7a-b displays the rising trajectory of two bubbles with 6 mm rising in non-Newtonian fluids at low flow index (n = 0.1) and high flow index (n = 0.9), respectively. As shown in Fig. 7a, when the bubbles with initial diameter 6 mm and flow index of n = 0.1 rose in the column, the bubbles shape changed from spherical to wobbling shape and the they began to deviate from each other in the horizontal direction. Whereas for the case of n = 0.9, the bubbles shape changed from spherical to ellipsoidal and the rising trajectory was shown nearly a straight path (see in Fig. 7b).

Fig. 8a-b illustrates the velocity fields around the bubbles at low flow index (n = 0.1) and high flow index (n = 0.9), respectively. For n = 0.1, at the time t = 0.05s, it is observed that a stronger circulation of vortexes cause between the bubbles gap that push

the bubbles edge. As a result, the bubbles shape changes to an oblate ellipsoidal disk (oed) shape at t = 0.1s. When the time is increased to 0.2s, the oed shape again changes to wobbling shape, which is attributed to the stronger shearing-thinning effect of non-Newtonian fluid. Note that, an excess vortex is seen at t = 0.2s. This excess vortex may be the primary reason for the deviation of the bubbles from each other in the horizontal direction (see Fig. 7a at t = 0.2 - 0.5s). Whereas, weak circulations happen between the bubbles gap for the case with flow index of n = 0.9, which are not able to push bubbles boundaries. Therefore, the shape of bubbles does not face too much change, as can be seen in Fig. 8b.

Fig. 9a-d shows the bubble horizontal interval ratio, bubble aspect ratio, bubble rising velocity and static pressure on bubble, respectively at three different flow indexes of n = 0.1, 0.5 and 0.9. In addition, the results of Fan et al. [25] for a pair of 6 mm bubble rise behavior when h* = 1.7, which are close to that in the present study, for carboxymethyl cellulose (CMC) solution of n = 0.904 is also included in Fig. 9a. Comparing Fan et al. [25] with the present study, on average, the results are quite close to one another; some differences are observed and this may have resulted due to the difference in the non-Newtonian fluid properties used, whereby Fan et al. [25] is based on CMC solution and the present study is based on xanthan gum solution. For example, in comparing n = 0.904 of Fan et al. [25] and n = 0.9 from present study, the maximum difference is about 9%. However, the horizontal interval ratio between the bubbles remains unchanged until t = 0.25s for n = 0.1 – 0.9. After that, the values of interval ratio of the non-Newtonian fluid with n = 0.1 increases dramatically, indicating high repulsion effects between the bubbles. However, much lower values were obtained for the fluid with n = 0.5 and 0.9, along with a similar trend for them.

Additionally, the flow index alters on bubble aspect ratio (or bubble shape) as shown in Fig. 9b. It is observed that the curve fluctuates severely the fluid at fluid with n = 0.1, but less fluctuation was observed at high flow index n = 0.5. When the flow index increased to n = 0.9, the variation of the bubble shape was not so remarkable, compared to the case of n = 0.1. The changes of bubble shape happened due to the development of stronger push of fluid jet around the bubble in bubble gap (see in Fig. 8a). Accordingly, Fig. 9c shows that the bubble rising velocity increases with decrease of n. This is may be related to shearing-thinning effects in non-Newtonian fluids, which reduced the viscosity of the fluid around the bubble gap, thus the rising resistance of the bubbles was faster in both vertical and horizontal directions.

Fig. 9d shows the effect of flow index on bubble static pressure with time. It has also been found that the static pressure decreases with increase of 'n' and time. Comparing three different n, on average, the results are relatively close to each another; but some differences are seen from t = 0.2s to 0.5s and this may have resulted due to start of strong shearing-thinning. For example, comparing n = 0.1 and 0.9, the maximum difference is about 16% on average from t = 0.2s - 0.5s. Subsequently, Fig. 10 shows the normalized static pressure as a function of bubble position in column. The static pressure and bubble position is normalized by atmospheric pressure and column height, respectively. The results shows the normalized static pressure decreases with the height of the bubble in the column and maximum differences is found to be less than 6% for the cases of different flow index (n) and different initial bubble interval (h*).

3.3 Effect of oblique angle θ between bubble pairs at different flow index

In this section, the bubbles pair with non-horizontal configurations has been investigated. The simulation results reveal that on the rising process, bubble path and bubble interval would experience a huge variation at different oblique alignments. The oblique configuration between two bubbles is shown in Fig. 11. The contours of bubbles shape with the variation of time for three initial angles θ = 10°, 22.5° and 45° and n=0.1 and 0.9, are shown in Fig. 12a-d. By considering the identical horizontal distance of h* = 2.0, it is manifested that when the configuration angle θ increases, the interaction between the two bubbles alters from repellence to attraction. This behavior can be observed with the comparison of Fig. 12a and 12b. Finally the bubbles are coalesced to each other by increasing θ to 45^o for both flow index n = 0.1 and 0.9 of non-Newtonian fluid, as displayed in Fig. 12c and 12d, respectively. The velocity fields around the bubbles at the beginning stage for different θ and low flow index n = 0.1 are displayed in Fig. 13a-c. From Fig. 13a, for small angle (θ = 10°), when the bubbles begin moving, the lower surface of the bubbles is pushed up by vortexes. The upper portion of the following bubble encounters to a negligible wake developed behind the lower surface of the upper bubble. As a result, the upper bubble has experienced a stronger pushed-away effect by the following bubble. Thus, the both bubbles shapes deform significantly and their rising paths deviate gradually from the original vertical line, resulting in enlargement of the bubble distance. The pushed-away effect gradually gets weaker (or wake effect gradually gets stronger) behind the upper bubble with increasing θ from 22.5^o (see in Fig. 13b) to 45^o (see in Fig. 13c).

The bubble horizontal interval ratio and the change of angle between the centre line of the bubbles and horizontal direction at three different initial angles (θ = 10°, 22.5° and 45°) with three

different flow indexes (n = 0.1, 0.5 and 0.9) are illustrated in Fig. 14 and Fig. 15, respectively. According to Fig. 14a and 14b, at low flow indexes (i.e., n = 0.1 and n = 0.5), fluid generates a stronger repulsive effect for the cases with θ = 10° and 22.5° respectively. Consequently, higher values of interval ratio are obtained as compared to the highest flow index (n = 0.9). The stronger repulsive effect is generated at horizontal direction due to the stronger shear thinning effect. In addition, the results of Fan et al. [25] for an initial angle of 17° when h* = 1.7, which is close to that in our simulation of 22.5°, is also included in Fig. 14b. Comparing between Fan et al. [25] and the present study, some differences are seen because of two differences non-Newtonian fluid properties as earlier discussed. For example, in comparing n = 0.904, θ = 17° of Fan et al. [25] and n = 0.9, θ = 22.5° from present simulation, the maximum difference is about 13%.

When θ = 45° (see Fig. 14c), the decreasing trend of curves represents the weaker repulsion effect for the three different flow indexes (n). Additionally, the value of interval ratio (ΔX/Xi) of zero for the three different *n* represents the coalescence of the bubbles. Our result shows noticeable differences with the results of Vélez-Cordero et al. [23]; who found that the bubbles have an attraction and repulsion behavior at θ = 42° for n = 0.5 - 0.8. Moreover, as the θ increased at 61° and 78°, the bubbles have been coalescent with each other for n = 0.5 and 0.7, but no coalescence can be found for n = 0.8. In contrast to this results, our study has showed only the bubble coalescence at θ ≥ 45° for n = 0.1 - 0.9. This may be explained from relatively low physical properties of the pure xanthan gum solutions that facilitates the attraction behaviour of bubble coalescence, while the higher physical properties of mixture solutions (i.e., xanthan gum and glycerine/water) showed both attraction/coalescence and repulsion phenemonen. [23]

Fig. 15a-c shows the variations of configuration angle against time for various flow indexes. For the first two graphs (θ =10° and 22.5°), the curves related to both flow indexes of n = 0.1 and 0.5 experienced a sudden drop after the time step around t = 0.25s , indicating that the shear thinning effect is strong enough to change bubble angle configuration, while less changes observed for the curves with n = 0.9. But for the initial angle of θ = 45°, the configuration angle curve increases steeply for flow index n = 0.9 and 0.5 with no fluctuation (see in Fig. 15c). Moreover, as indicated in above, a fluctuated configuration angle is seen for n = 0.1 due to its higher shear thinning effect. It is worth to mention that the end of each curve represents the bubbles coalescence time at t = 0.30s approximately for θ = 45° (see in Fig. 15c). By comparing that for small angle, there always exists a repulsive effect between the bubbles in both directions as well as the variation of angle for the low flow index of 0.1 - 0.5 non-Newtonian fluid; whereas for large angle, an attraction between bubbles is stronger than the repulsive effect. In the other word, the bubble repulsion effect can be controlled by using initial oblique angle variation.

The velocity flow fields, outside and inside pressure profile on the bubbles before starting of coalescence (t = 0.30s) for low flow index n = 0.1 and high flow index n = 0.9 are also displayed in Fig. 16a-b, respectively. For both flow indexes, the horizontal attraction between the bubble pair increases which resulting it to move closer to each other and subsequently coalesce at t = 0.30s. It is noted that in case of n = 0.1 (or Fig. 16a), the upper surface of trailing (or following) bubble moves quicker due to the wake (or low pressure region) created by the upper bubble (refer to the outside pressure profile in Fig. 16a). While the lower surface of the trailing (or following) bubble is altered significantly as a reason of stronger vortex of fluid (see velocity flow field in Fig. 16a) for n = 0.1, which is caused due to the high pressure region (see in the outside

pressure profile in Fig. 16a) as compared to the velocity flow field for a higher flow index of n = 0.9 (see in Fig. 16b). However, a noticeable difference in value between the outside and inside bubble pressure can be found for n = 0.1, e.g., the upper and trailing bubble pressure differences are 29.8 Pa and 97 Pa, respectively. But, for n = 0.9, the upper bubble pressure difference is 1.5 Pa, which means that a less deformation of the bubble, while the pressure difference of 40.24 Pa represents a relatively more deformation of the trailing bubble. So, it can be attributed to the reduction of viscosity at local region produced by shear-thinning effect of the wake behind the upper bubble as well as higher pressure difference on the bubble, which results in more deformation of the bubble.

4. Conclusion

The dynamical characteristics of a pair of bubbles rising through non-Newtonian fluids were simulated numerically by VOF method. The conclusions of this study are drawn as below:

- In horizontal configuration, the interaction between bubble pairs in non-Newtonian fluids shows repulsive effect which increases with decreasing the initial center-to-center distance of bubbles due to the reduction of shear-thinning properties of fluid. This leads to intensification of vortexes between the bubbles gap as well as a strong push-away effect between them.
- For oblique angle configuration of a pair of bubbles, it was found that there is a repulsive effect between the bubbles as the $\theta < 45^{o}$. While initial angle configuration of $\theta > 45^{o}$ shows an attraction between the bubbles, which results in the collision of them in a wide range of flow index, n ~ 0.1 - 0.9.
- Flow field around the rising bubbles experiences significant changes with the variation of flow

index which can bring about a noticeable difference of rising velocities between them. In addition, as the flow index decreases, a dramatic oscillation is occurred between the bubbles and their shape alters from spherical to wobbling shape.

Acknowledgements

This research is financially supported by University of Malaya, Ministry of Higher Education High Impact Research (UM.C/HIR/MOHE/ENG/20), and University of Malaya Research Grant (UMRG: RG121/11AET).

References

1. N. Kantarci, F. Borak and K. O. Ulgen, *Process Biochemistry*, 2005, **40**, 2263-2283.
2. N. Yang, Z. Wu, J. Chen, Y. Wang and J. Li, *Chemical Engineering Science*, 2011, **66**, 3212-3222.
3. M. Pourtousi, J. Sahu and P. Ganesan, *Chemical Engineering and Processing: Process Intensification*, 2014, **75**, 38-47.
4. Z. Cai, Y. Bao and Z. Gao, *Chinese Journal of Chemical Engineering*, 2010, **18**, 923-930.
5. V. Badam, V. Buwa and F. Durst, *The Canadian Journal of Chemical Engineering*, 2007, **85**, 257-267.
6. S. D. Bari and A. J. Robinson, *Experimental Thermal and Fluid Science*, 2013, **44**, 124-137.
7. P. Di Marco, N. Forgione and W. Grassi, Congresso Nazionale UIT sulla Trasmissione del Calore, 2005.
8. X. Zhang, H. Dong, D. Bao, Y. Huang, X. Zhang and S. Zhang, *Industrial & Engineering Chemistry Research*, 2013, **53**, 428-439.
9. H. Dong, X. Wang, L. Liu, X. Zhang and S. Zhang, *Chemical Engineering Science*, 2010, **65**, 3240-3248.
10. L. Parkinson, R. Sedev, D. Fornasiero and J. Ralston, *Journal of colloid and interface science*, 2008, **322**, 168-172.
11. W. Fan, S. Jiang, C. Zhu, Y. Ma and H. Li, *Optics & Laser Technology*, 2008, **40**, 389-393.
12. J. Herrera-Velarde, R. Zenit, D. Chehata and B. Mena, *Journal of non-newtonian fluid mechanics*, 2003, **111**, 199-209.
13. T. Miyahara and S. Yamanaka, *Journal of chemical engineering of Japan*, 1993, **26**, 297-302.

14. H. A. Jakobsen, H. Lindborg and C. A. Dorao, *Industrial & engineering chemistry research*, 2005, **44**, 5107-5151.
15. X. YUAN and G. YU, *Chinese Journal of Chemical Engineering*, 2008, **16**, 497-502.
16. O. Hassager, 1979.
17. T.-J. Lin and G.-M. Lin, *Chemical Engineering Journal*, 2009, **155**, 750-756.
18. R. C. COKE, R. NAGEL and R. ETCHEVERRY, *The Canadian Journal of Chemical Engineering*, 2008.
19. H. Z. Li, X. Frank, D. Funfschilling and Y. Mouline, *Chemical Engineering Science*, 2001, **56**, 6419-6425.
20. N. Hassan, M. M. K. Khan and M. Rasul, *WSEAS Trans. Fluid Mech*, 2008, **3**, 261.
21. T. Sanada, A. Sato, M. Shirota and M. Watanabe, *Chemical Engineering Science*, 2009, **64**, 2659-2671.
22. D. Legendre, J. Magnaudet and G. Mougin, *Journal of Fluid Mechanics*, 2003, **497**, 133-166.
23. J. R. Vélez-Cordero, D. Sámano, P. Yue, J. J. Feng and R. Zenit, *Journal of Non-Newtonian Fluid Mechanics*, 2011, **166**, 118-132.
24. W. FAN, Y. MA, X. LI and H. LI, *Chinese Journal of Chemical Engineering*, 2009, **17**, 904-913.
25. W. FAN and X. YIN, *Chinese Journal of Chemical Engineering*, 2013, **21**, 705-713.
26. Z. Yu, H. Yang and L.-S. Fan, *Chemical Engineering Science*, 2011, **66**, 3441-3451.
27. M. Cheng, J. Hua and J. Lou, *Computers & Fluids*, 2010, **39**, 260-270.
28. L. Zhang, C. Yang and Z.-S. Mao, *Journal of Non-Newtonian Fluid Mechanics*, 2010, **165**, 555-567.
29. M. Ohta, E. Iwasaki, E. Obata and Y. Yoshida, *Journal of non-newtonian fluid mechanics*, 2003, **116**, 95-111.
30. Z. Yu and L. S. Fan, *The Canadian Journal of Chemical Engineering*, 2008, **86**, 267-275.
31. J. Liu, C. Zhu, T. Fu and Y. Ma, *Industrial & Engineering Chemistry Research*, 2014, **53**, 4850-4860.
32. J. Liu, C. Zhu, T. Fu, Y. Ma and H. Li, *Chemical Engineering Science*, 2013, **93**, 55-66.
33. M. van Sint Annaland, W. Dijkhuizen, N. Deen and J. Kuipers, *AIChE Journal*, 2006, **52**, 99-110.
34. J. P. Singh and M. M. Denn, *Physics of Fluids (1994-present)*, 2008, **20**, 040901.
35. J. Tsamopoulos, Y. Dimakopoulos, N. Chatzidai, G. Karapetsas and M. Pavlidis, *Journal of Fluid Mechanics*, 2008, **601**, 123-164.
36. G. K. Batchelor, *An introduction to fluid dynamics*, Cambridge university press, 2000.
37. C. W. Hirt and B. D. Nichols, *Journal of computational physics*, 1981, **39**, 201-225.
38. J. Brackbill, D. B. Kothe and C. Zemach, *Journal of computational physics*, 1992, **100**, 335-354.
39. E. C. Bingham, 1922.
40. D. Ma, M. Liu, Y. Zu and C. Tang, *Chemical Engineering Science*, 2012, **72**, 61-77.
41. K. Dewsbury, D. Karamanev and A. Margaritis, *Chemical engineering science*, 1999, **54**, 4825-4830.
42. A. Margaritis, D. W. te Bokkel and D. G. Karamanev, *Biotechnology and bioengineering*, 1999, **64**, 257-266.

43. D. Youngs, *Numerical methods for fluid dynamics*, 1982, **24**, 273-285.

LIST OF FIGURES

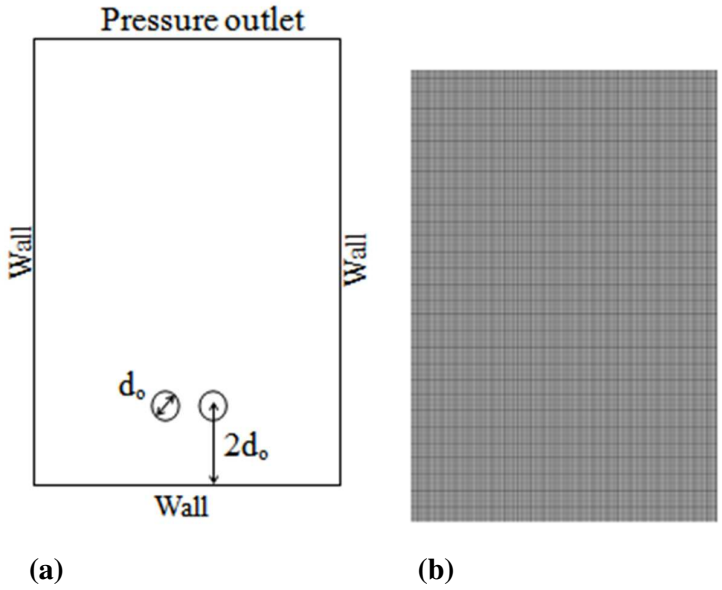

Fig. 1 (a) Physical model of the computational domain and (b) uniform structured grid.

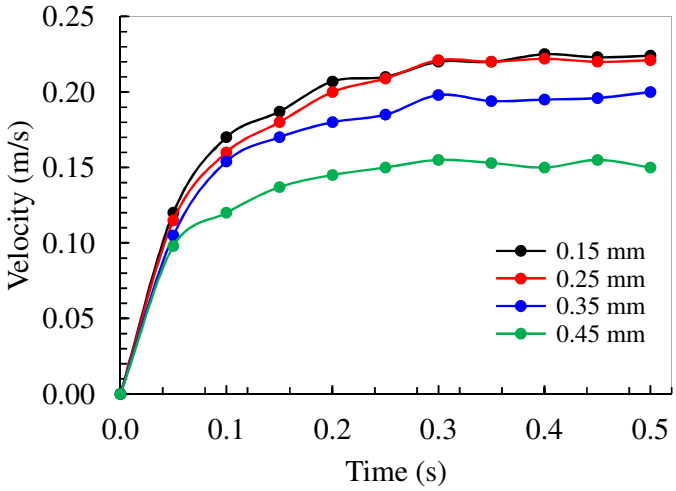

Fig. 2 Effect of mesh interval size on 6 mm bubble rising velocity.

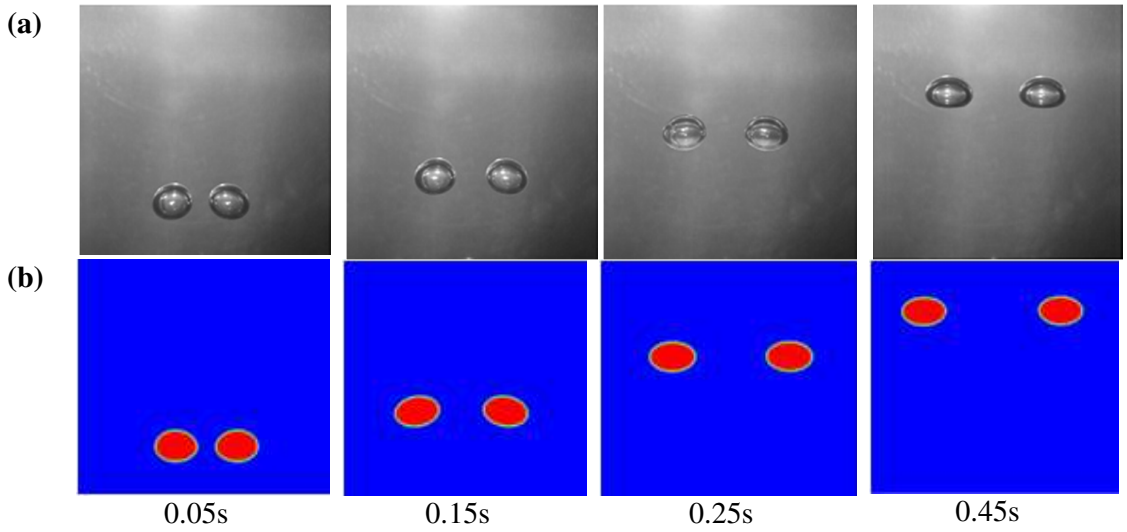

Fig. 3 Comparisons of rising of two parallel bubbles and shape between (a) experiment shape of bubbles from Lui et al. [32]; (b) present simulation.

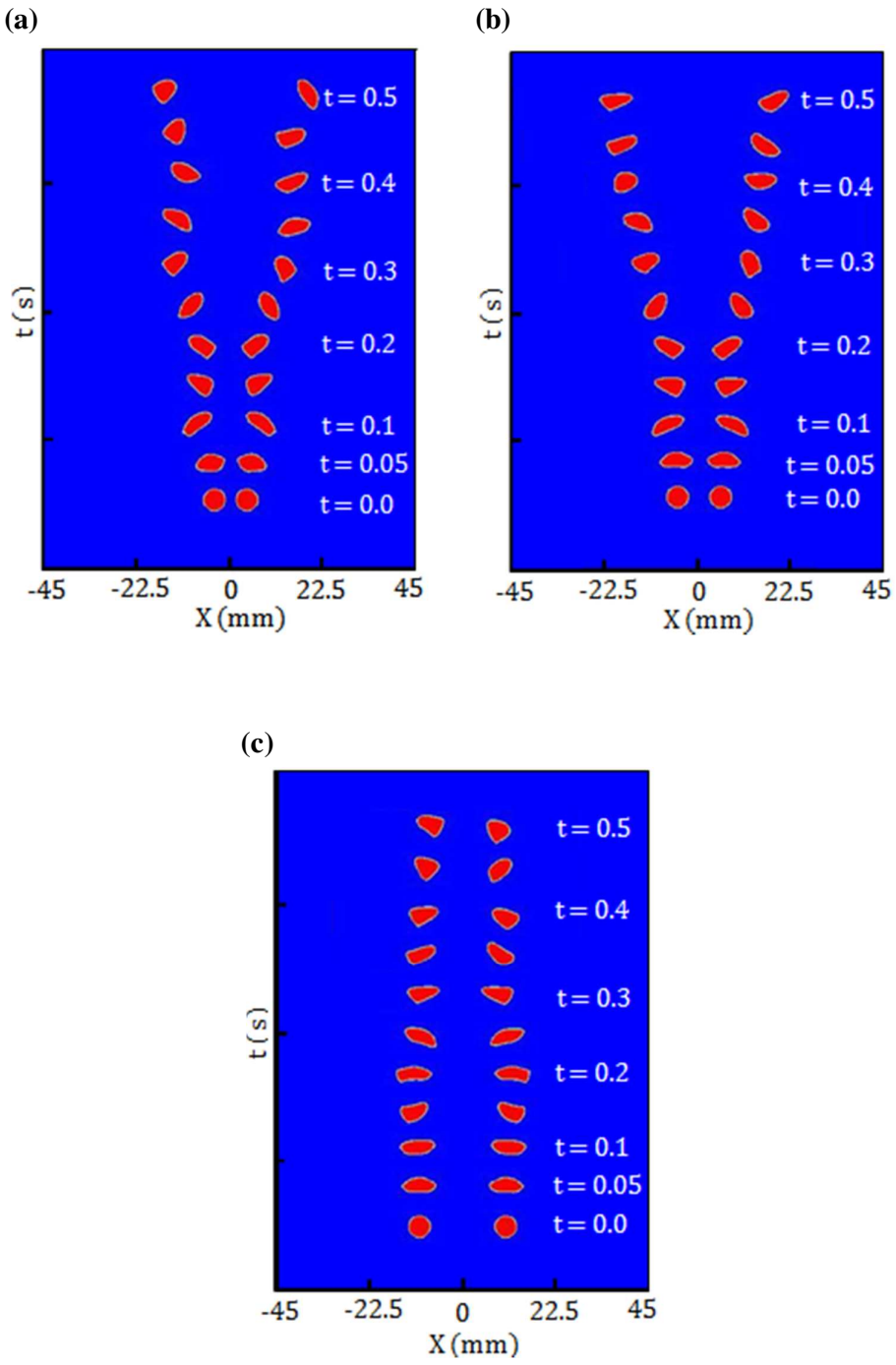

Fig. 4 Two parallel bubble rising trajectory at different initial interval when flow index, n = 0.5, (a) h* =1.5; (b) h* = 2.0; (c) h* = 4.0.

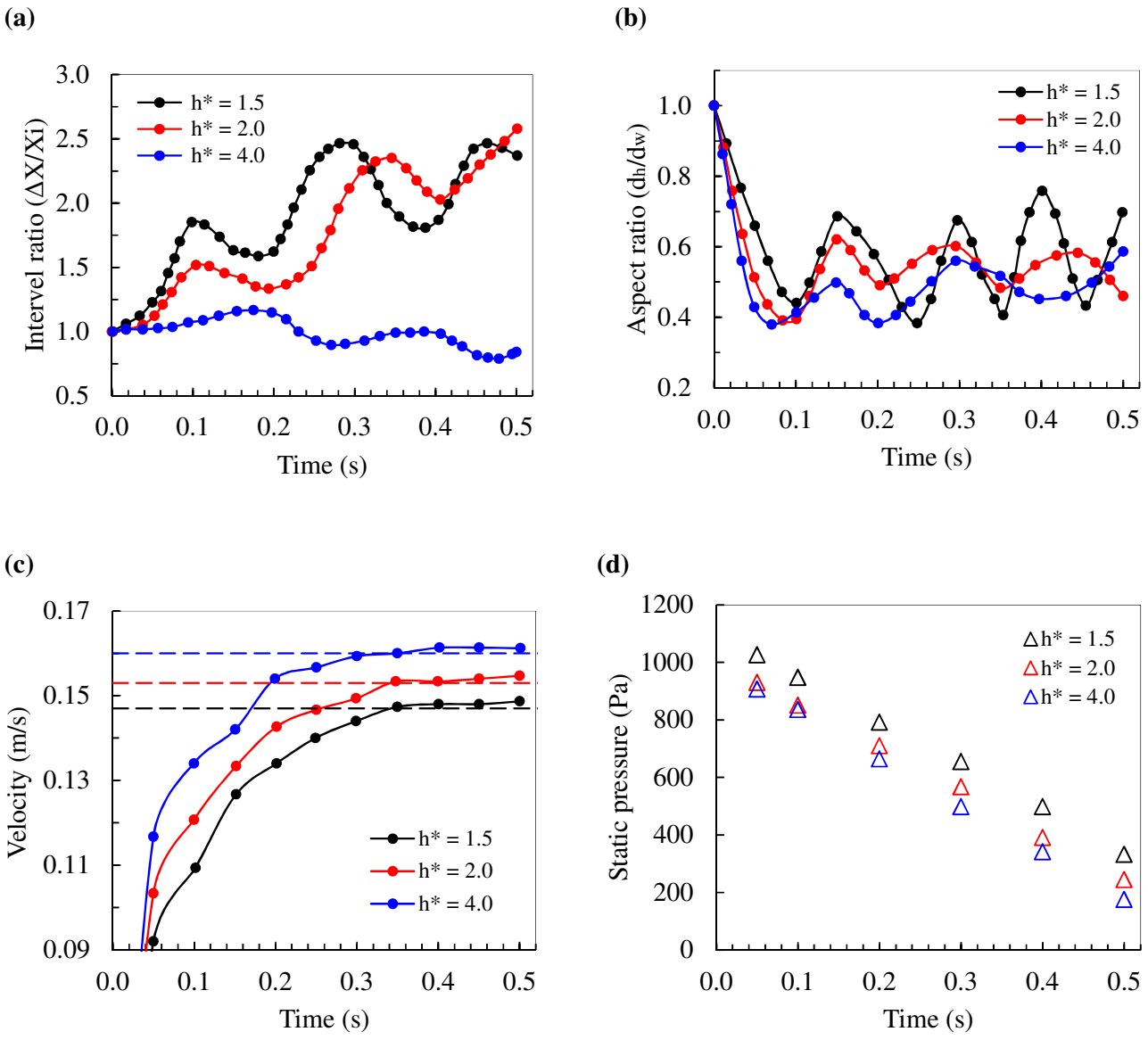

Fig. 5 (a) Bubble interval ratio; (b) bubble aspect ratio; (c) bubble rising velocity and (d) static pressure as a function of time at different initial bubble interval.

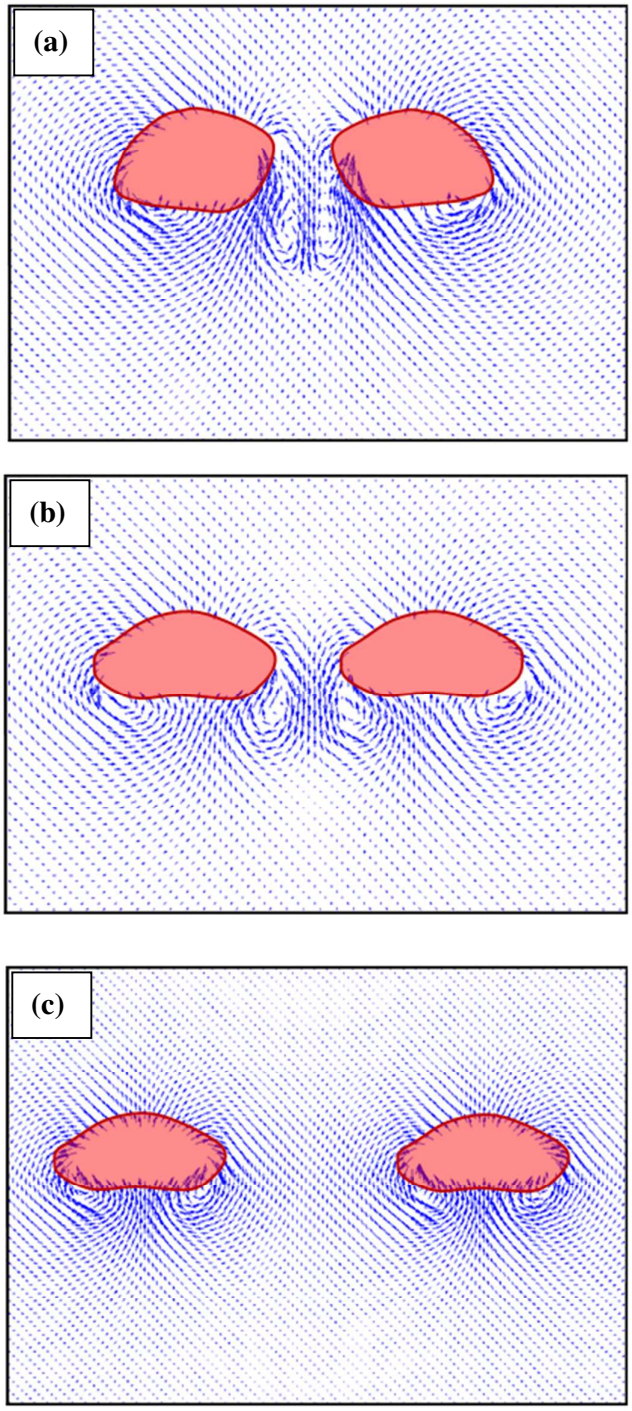

Fig. 6 Velocity flow field around rising bubble pairs at t = 0.05s and n = 0.5; when (a) h* = 1.5; (b) h* = 2.0; (c) h* = 4.0.

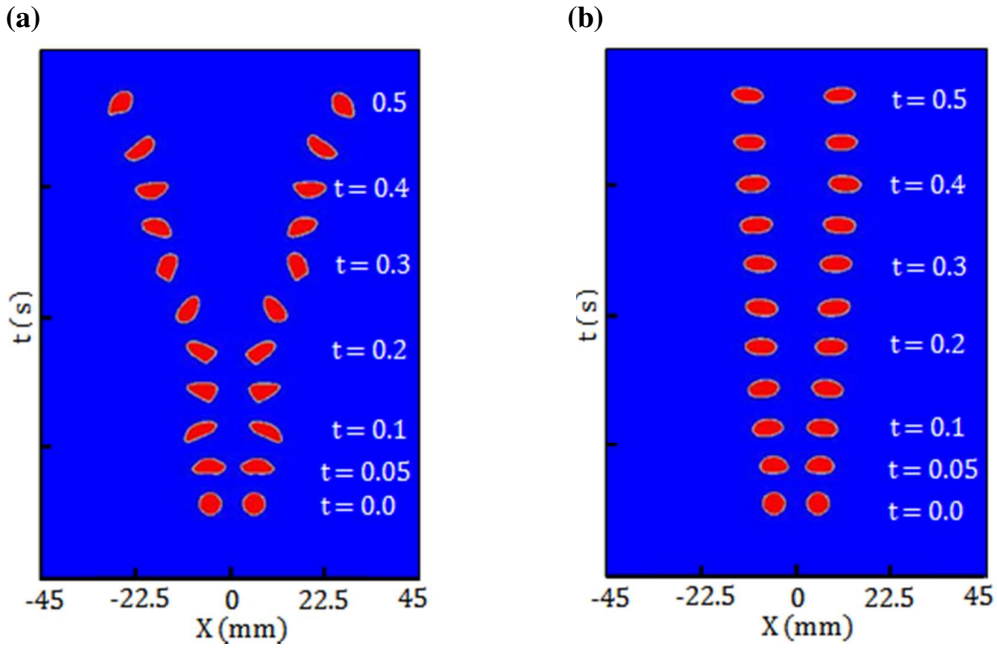

Fig. 7 Trajectory of 6 mm bubble at (a) low flow index, n = 0.1 and (b) high flow index, n = 0.9.

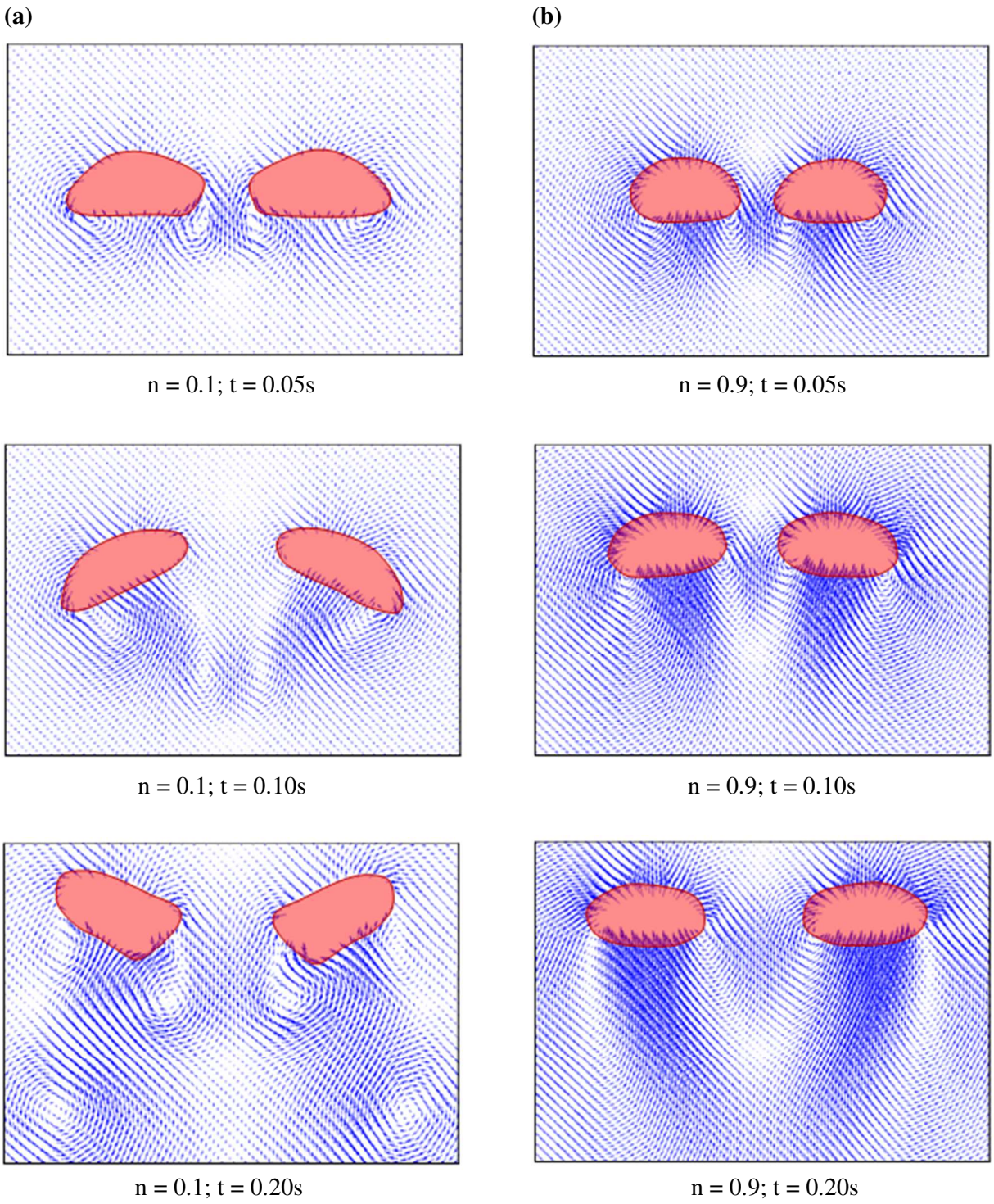

Fig. 8 Velocity field abound the bubble at different time when h* = 2, (a) low flow index, n = 0.1; (b) high flow index, n = 0.9.

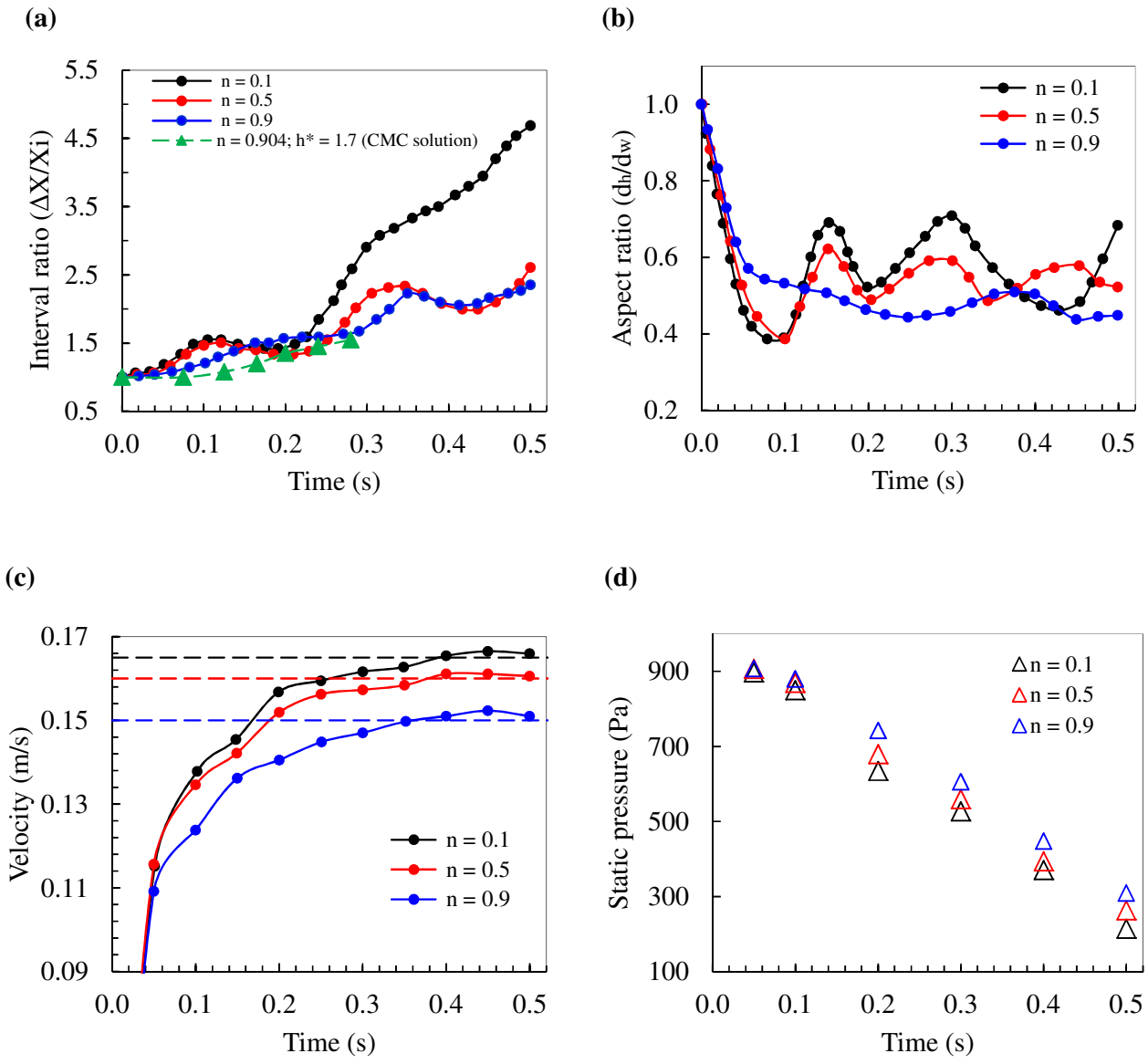

Fig. 9 (a) Bubble interval ratio and such data of CMC solution from Fan et al. [25] is also included; (b) bubble aspect ratio; (c) bubble velocity and (d) static pressure as a function of time at different flow index n, when h* = 2.0 and do = 6 mm.

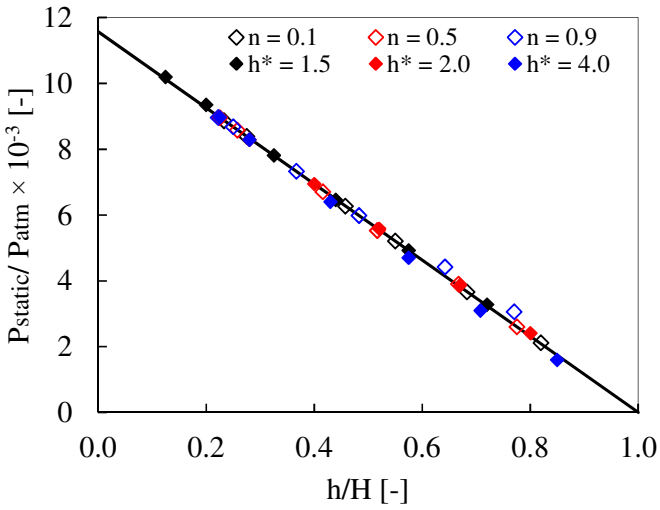

Fig. 10 Normalized static pressure as a function of bubble position at different flow index n and different initial bubble interval.

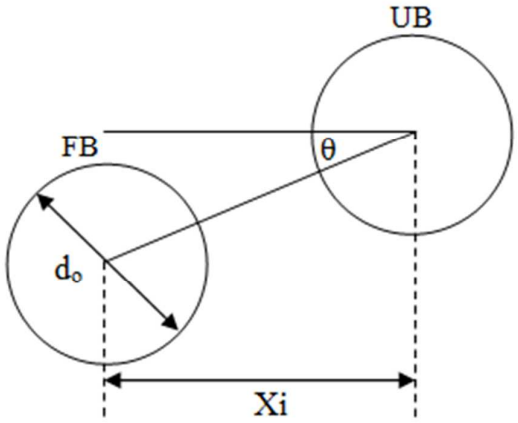

Fig. 11 Schematics of the configuration of a bubble pair; Noted: FB and UB means following bubble and upper bubble, respectively.

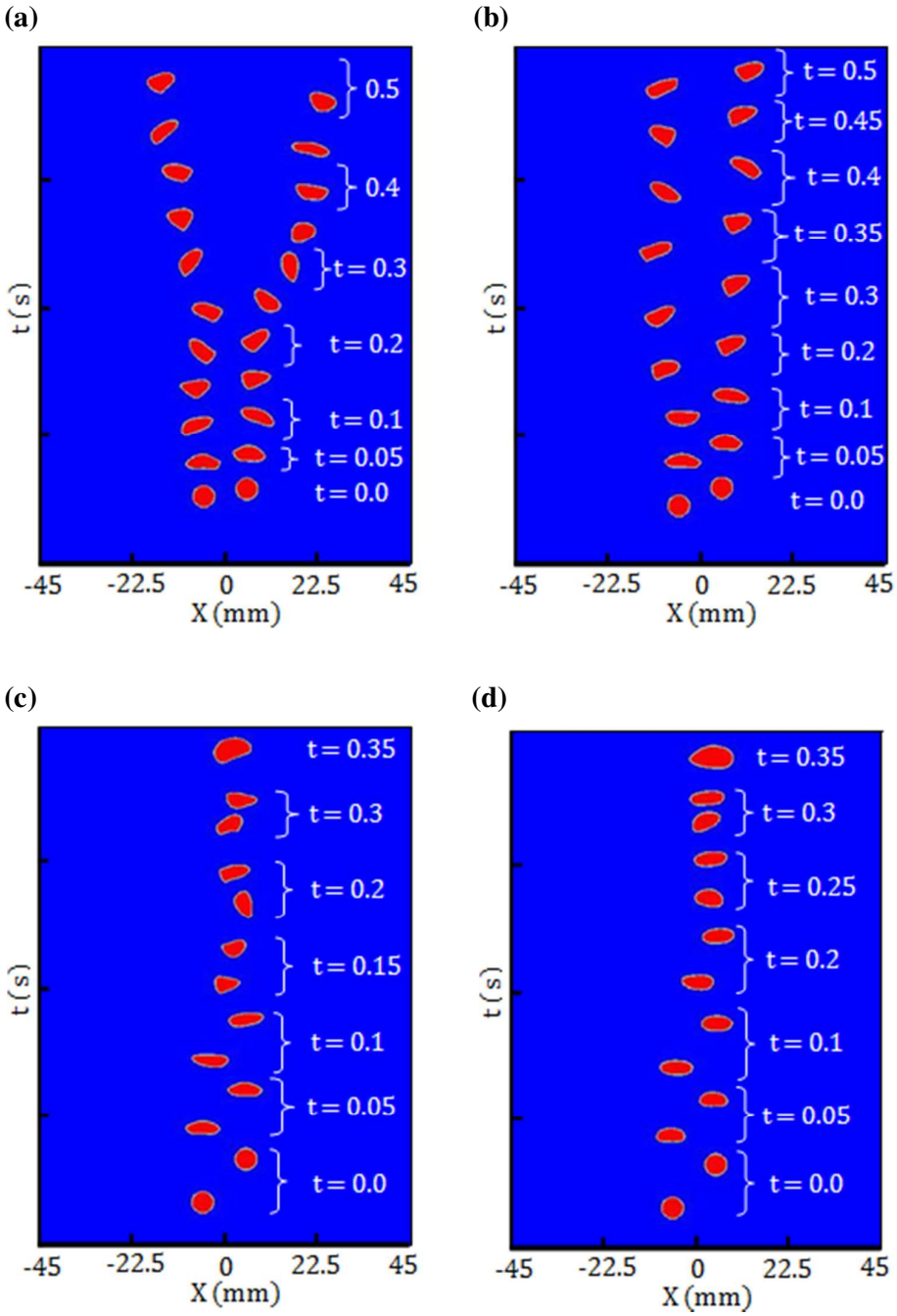

Fig. 12 Bubble rising trajectory at different angle when h* = 2, (a) β=10°, n = 0.1; (b) β=22.5°, n = 0.1; (c) β=45°, n = 0.1 and (d) β=45°, n = 0.9.

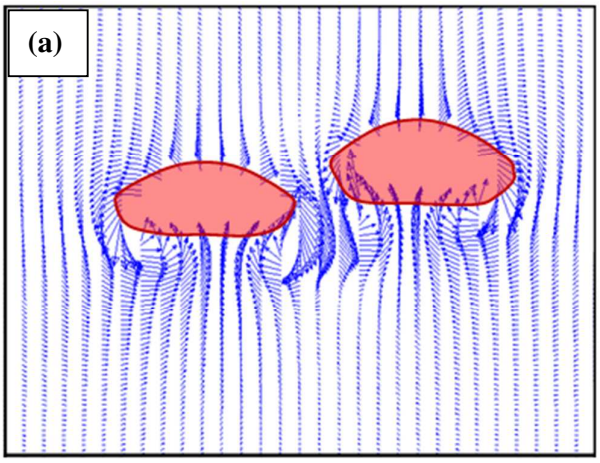

θ =10°, n = 0.5, t = 0.05s

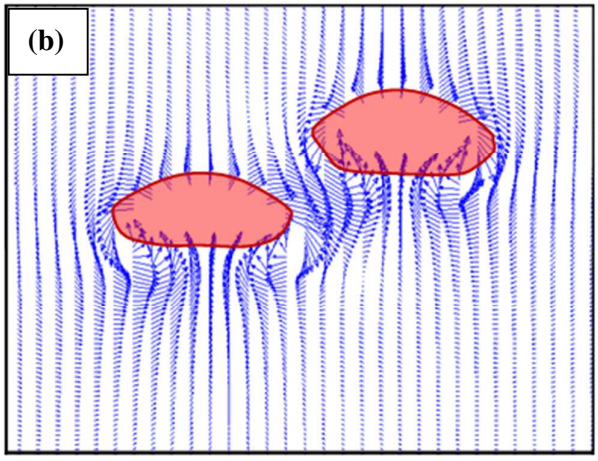

θ = 22.5°, n = 0.5, t = 0.05s

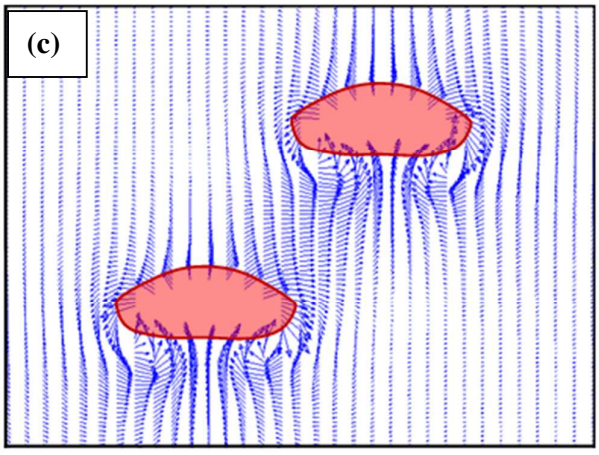

θ = 45°, n = 0.5, t = 0.05s

Fig. 13 Velocity flow field around rising of 6 mm bubbles at n = 0.1 and t = 0.05s, when the oblique angle (a) θ =10°; (b) θ = 22.5°; (c) θ = 45°.

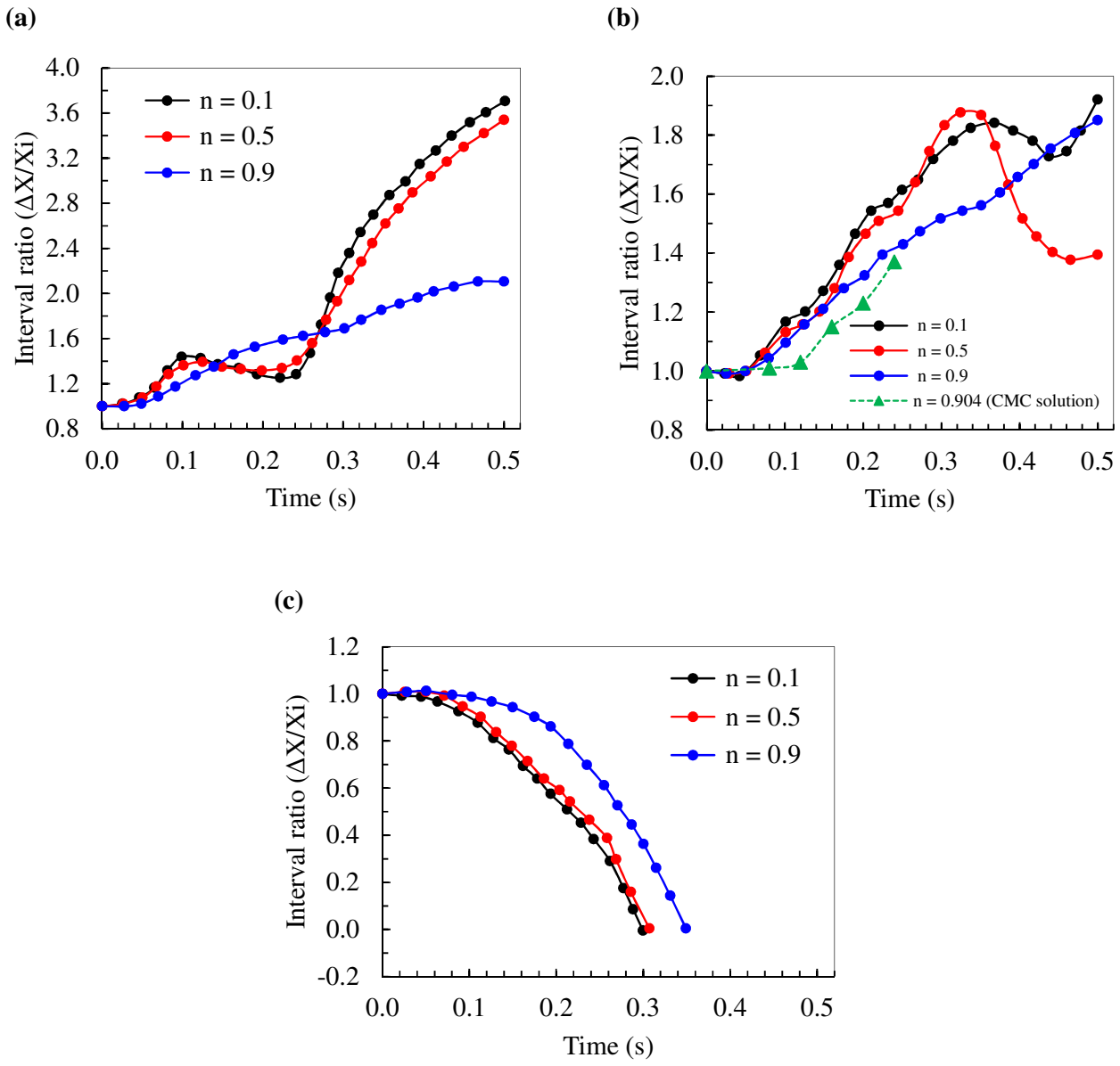

Fig. 14 6 mm bubble interval ratio as a function of time at different flow index n; (a) θ = 10°; (b) θ = 22.5°; such data of CMC solution from Fan et al. [25] is also included for θ = 17°; (c) θ = 45°

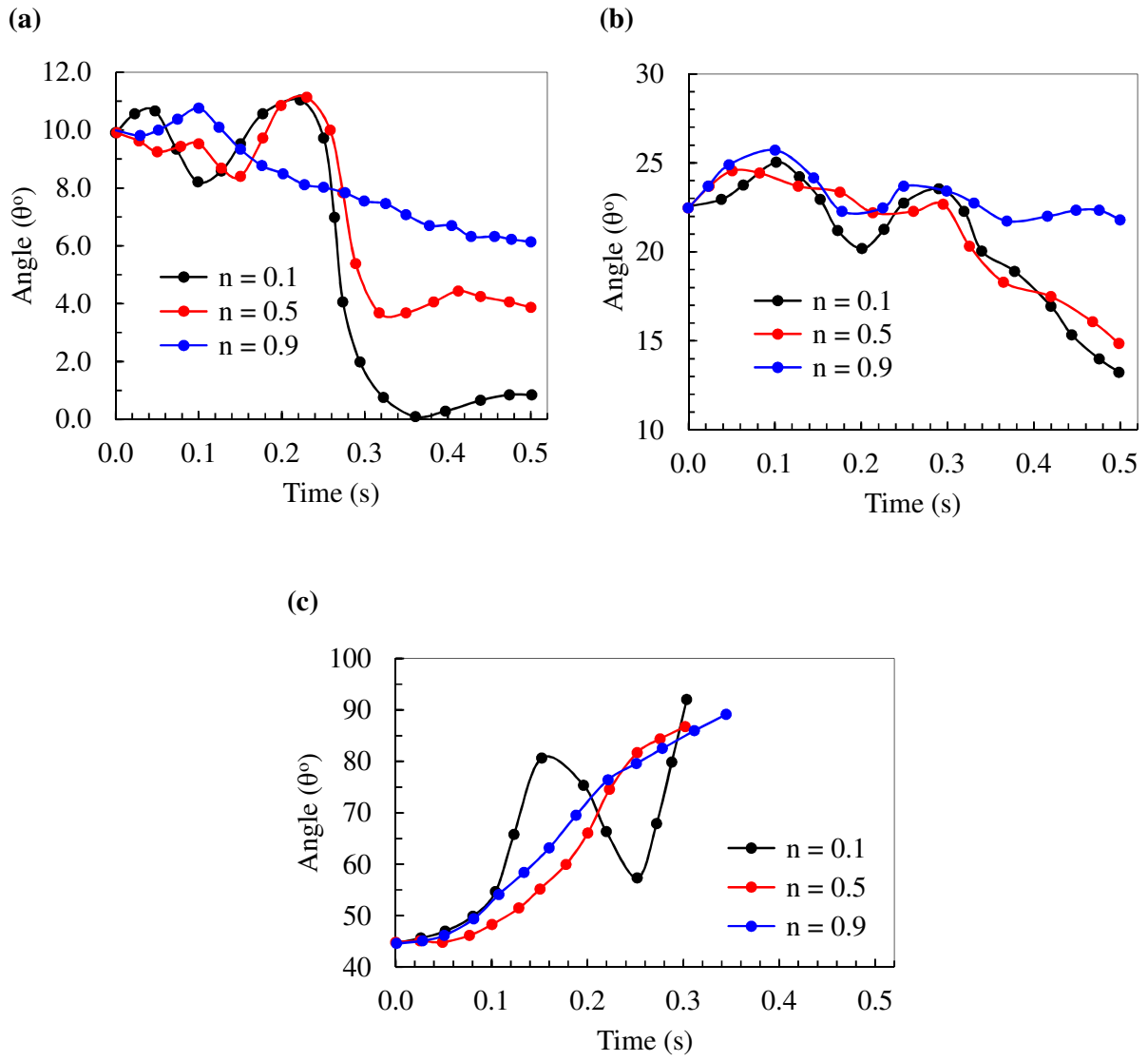

Fig. 15 Variation of angles as a function of time at different flow index n; (a) θ = 10°; (b) θ = 22.5°; (c) θ = 45°.

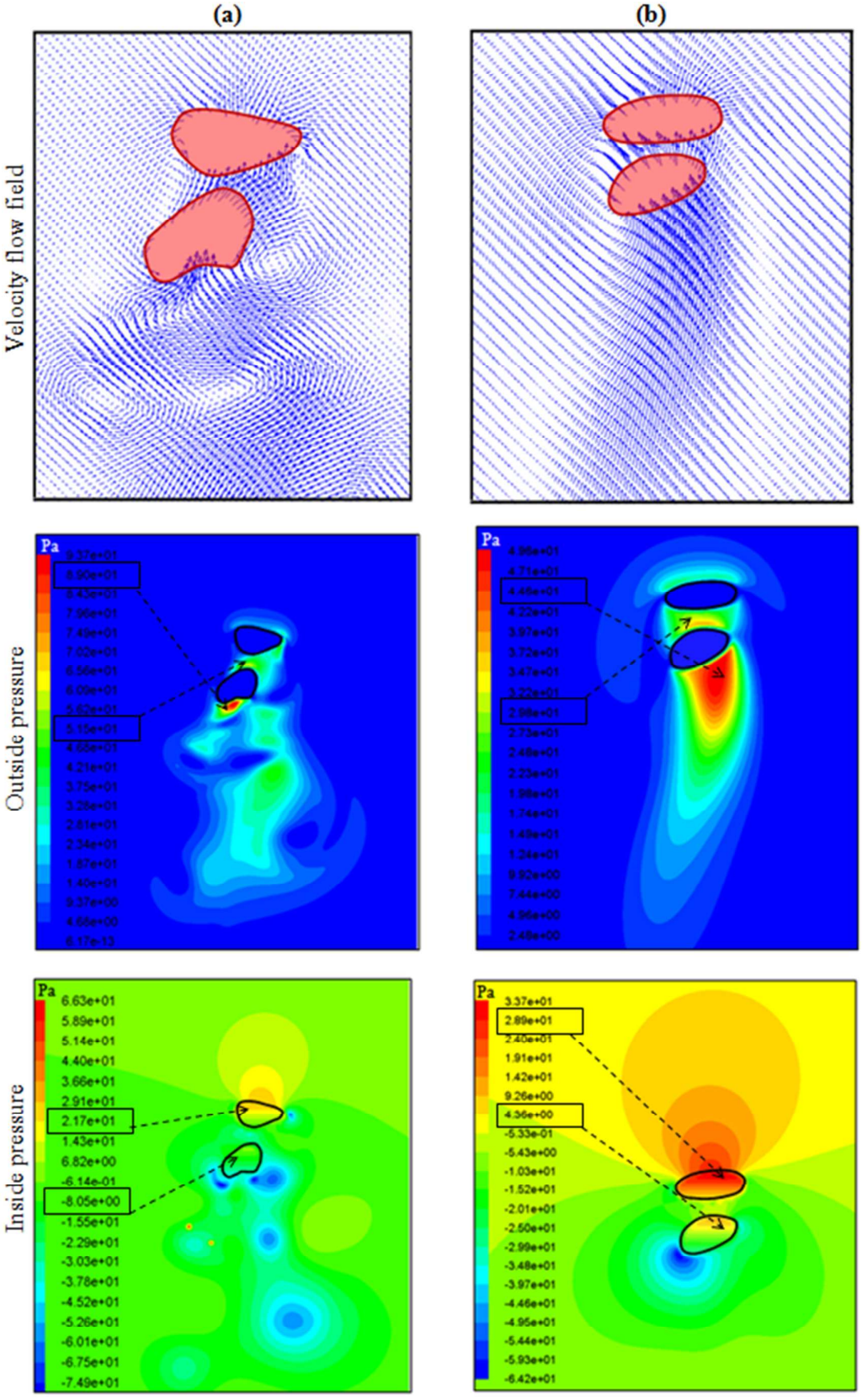

Fig. 16 Velocity flow field, outside and inside pressure profile on the rising of 6 mm bubble before coalescence at t = 0.30s and θ = 45°, when (a) low flow index, n = 0.1; (b) high flow index, n = 0.9.

LIST OF TABLES

Table 1: Comparisons of equivalent diameter (d_e); bubble rising velocities (U_T) and Reynolds number between experiment and present simulation.

	d_e (mm)	U_T (m/s)	d_h/d_w	Re [-]	Error of Re (%)
Two parallel bubbles					
Experimental [32]	4.1034	0.181	0.648	20.96	3.76
Simulation	4.213	0.172	0.636	20.17	
Single bubble					
Experimental [20]	6	0.231	[-]	77.75	2.43
Simulation	6.452	0.225	0.683	75.86	
Experimental [20]	10	0.242	[-]	107.32	1.22
Simulation	10.824	0.237	0.562	108.63	

Table 2 Simulation cases.

Case	ρ_l [kg/m^3]	K [Pa.s^n]	n [-]	h* [-]	θ [^{o}]	Purpose
1	1005.6	0.048	0.922	2.0	0	Validation of the simulation with the available leterature. [20, 32]
2	997	0.095	0.548	0.0		
3-5	997	0.095	0.5	1.5, 2.0, 4.0	0	To investigate the effect of horizontal interval between a pair of bubbles.
6-8	997	0.095	0.1, 0.5, 0.9	2.0	0	To investigate the effect of flow index (n) between a pair of bubbles rising dynamics.
9-17	997	0.095	0.1, 0.5, 0.9	2.0	10 22.5 45	To investigate the effect of oblique angle and flow index (n) between a pair of bubbles rising dynamics.